Applied Physics Letters

RESEARCH ARTICLE | JULY 24 2024

Observation of acoustic meron textures

Nong Zhou ; Wan-Na Chen ; Wen-Jun Sun ; Zong-Qiang Sheng ; Hong-Wei Wu

Appl. Phys. Lett. 125, 042204 (2024)
https://doi.org/10.1063/5.0217864

AIP Publishing

Applied Physics Letters ARTICLE pubs.aip.org/aip/apl

Observation of acoustic meron textures

Cite as: Appl. Phys. Lett. **125**, 042204 (2024); doi: 10.1063/5.0217864
Submitted: 7 May 2024 · Accepted: 14 July 2024 ·
Published Online: 24 July 2024

Nong Zhou,[1] Wan-Na Chen,[1] Wen-Jun Sun,[1] Zong-Qiang Sheng,[1] and Hong-Wei Wu[1,2,3,a)]

AFFILIATIONS

[1]School of Mechanics and Photoelectric Physics, Anhui University of Science and Technology, Huainan 232001, China
[2]Center for Fundamental Physics, Anhui University of Science and Technology, Huainan 232001, China
[3]Institute of Energy, Hefei Comprehensive National Science Center (Anhui Energy Laboratory), Hefei 230031, China

[a)]Author to whom correspondence should be addressed: hwwu@aust.edu.cn

ABSTRACT

Merons, as a member of quasiparticle family characterized by half-integer of the skyrmion topological charge with nontrivial topological textures, are of great interest in various branches of physics. Here, we report the first experimental observation of a meron texture configuration in acoustic waves. A squared metastructure is designed to support the spoof acoustic surface wave, forming meron lattice patterns in the acoustic velocity field vectors. The experimental results indicate that the meron textures can be moved and shaped by tuning the phase and amplitude differences between the excited sound sources, respectively. To demonstrate the topologically protected character of meron against structure defects, we further measure the acoustic pressure and velocity field distributions on a defective surface. The acoustic meron texture not only provides potential applications toward topologically robust ways to manipulate vectorial characteristics of the acoustic waves but also instills confidence for exploring other members of the quasiparticle family, such as the acoustic hopfion in acoustic waves.

Topological textures, which refer to nontrivial distributions of physical vector fields in real space, arouse great interest in different branches of physics, with various configurations such as vortices,[1,2] skyrmions,[3,4] merons,[5–7] and hopfions.[8,9] Skyrmion is a prominent topological texture, which is characterized by a real-space topological number (i.e., skyrmion number). The nontrivial topology of the skyrmion texture protects the vector field distribution against structure defect and intrusion. With advanced topological property, skyrmions in magnetic materials have grown into a large research field, giving rise to various topological textures, including Néel type,[10] Bloch type,[11] anti-type,[12] and so on. Topologically protected spin textures hold promise for applications in data manipulation for future spintronic devices. Recently, skyrmion vectorial textures are constructed in photonics for electric/magnetic fields,[13–15] spins,[16,17] and phononics for acoustic velocity field,[18–21] as well as water waves for instantaneous displacements of the water-surface particles.[22] These skyrmion-like textures discovered in classical waves unveil novel topological modes for linking the quantum systems and the classical wave systems, which may be useful in manipulation of vector fields of classical waves.

Meron, a vectorial texture characterized by half-integer of the skyrmion topological charge mapping from half three-dimensional (3D) spherical hypersurface as a kind of quasiparticle, is discovered in chiral magnetic materials,[23] optical system in real space,[13,24] and moment space.[25] Recently, with the development of the structured acoustic field, the vectorial properties and acoustic spin are deeply explored for acoustic waves.[26–31] The advancement in the knowledge of acoustic vectorial field holds promise for exciting opportunities to explore acoustic topological textures, such as skyrmionic lattice formations on a hexagonal acoustic metasurface,[18] tunable localized acoustic skyrmionic modes on acoustic metastructures,[19,20] and polarization singularities, topological Möbius-strip structures, and skyrmionic textures in 3D polarization fields of inhomogeneous sound waves.[32] However, as an indispensable member of the family of topological vectorial texture, acoustic meron and antimeron have not been reported in acoustic systems. The experimental realization of acoustic meron will provide confidence for constructing various topological textures in acoustic field and enrich applications in robust vectorial acoustic communication and data storage.

In this work, we experimentally observe that the Néel-type meron lattice configuration of acoustic velocity fields can be supported on a squared metastructure. The spoof acoustic surface waves, with their evanescent nature, are supported on the structure surface to form the meron and antimeron patterns in acoustic velocity field distributions. We demonstrate that the topological texture can be moved and shaped by controlling the phase and amplitude difference between the acoustic sources in our setup. We also experimentally observe the topological robustness of the meron pattern against structure defects by measuring the pressure and velocity fields. The acoustic meron texture not only provides potential applications toward topologically robust ways to manipulate vectorial characteristics of the acoustic waves but also provides confidence for exploring various topological textures in the acoustic domain, such as acoustic hopfion, acoustic knot, and so on.

We implement the acoustic meron modes by constructing a tetragonal lattice on a metasurface, and four speakers are placed at four corners of the structure to create interference of acoustic surface waves along the x and y directions for forming the meron mode as shown in Fig. 1(a). The square lattice consists of 400 individual cells, 20 in length and 20 in width. Figure 1(b) gives the details of the structure parameters as follows: the height of the unit cell $H = 36$ mm, lattice constant $a = 10$ mm, height of the square hole $h = 30$ mm, lattice model total side length $L = 200$ mm, and the side length of the square hole $b = 6$ mm. Spoof surface acoustic waves (SSAWs) can be formed by coupling the sound from speakers to the structure, the velocity field and pressure field of SSAWs on the structure surface are shown in Fig. 1(c). The color of the structure represents the pressure field distribution, and the arrow above the structure corresponds to the velocity field vector of the SSAWs. The SSAWs are generated by local oscillations inside a single hole and the intercoupling between adjacent holes, and the wave decays exponentially in the z direction into the air region. Their propagation characteristics are affected by geometric parameters. Thus, we also calculate the dispersion relationship of the structure with different h values along the high symmetry direction of the square lattice as shown in Fig. 1(d) by using the pressure acoustic model of commercial software COMSOL Multiphysics,[33]

$$k_{SSAW} = \frac{\omega}{c}\sqrt{1 + \left(\frac{b}{a}\right)^2 \tan^2\left(\frac{\omega}{c}h\right)}, \tag{1}$$

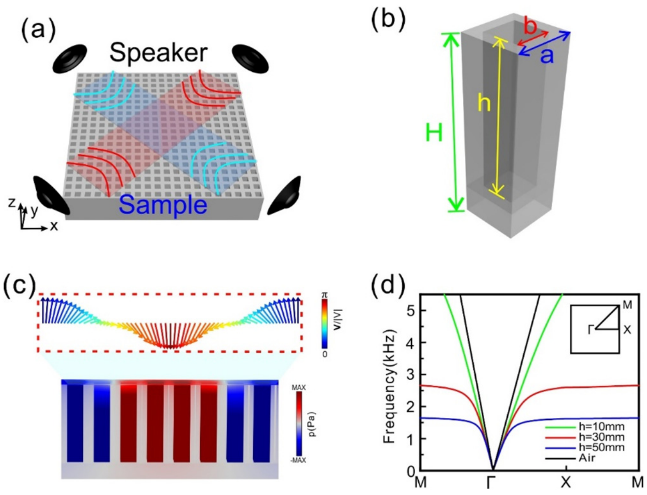

FIG. 1. Schematic structure and simulation results of the meron mode formed by the acoustic velocity field. (a) An acoustic metasurface with periodic perforations can be used to support the spoof surface acoustic waves (SSAWs), and acoustic meron lattice is excited by the interference of sound waves generated through the loudspeakers. (b) The unit-cell structure of the acoustic metasurface with structural parameters. (c) The sound velocity vector field propagates in a metasurface structure, and the direction is indicated by the arrow. (d) Dispersion curves at different depths of square holes with fixed side length $b = 6$ mm and lattice constant $a = 10$ mm. The upper right illustration shows the corresponding first Brillouin region.

where $\omega = 2\pi f$ is the angular frequency. The wave vectors' relation of SSAW satisfies $k_{SSAW}^2 - k_z^2 = k_0^2$, where k_z is the z component of the wave vector, and k_0 is the wave vector in free space.

In order to experimentally observe the acoustic meron lattice, we use 3D printing technology to make samples as shown in Fig. 2(a). Before starting the experimental measurement, we first simulate acoustic meron lattice based on the commercial software COMSOL Multiphysics in a pressure acoustic frequency domain module. We construct a lattice model of the same size and set the model as a resin material. The length of meron formed at the center of the structure is set to be l, and the distribution diagram of sound pressure field and velocity field of meron's eigenmode calculated are shown in Fig. 2(b). When we set the lattice constant $a = 10$ mm, the height of the square hole $h = 30$ mm, the side length of the square hole $b = 6$ mm, and the excitation frequency $f = 2200$ Hz, we can get $k_{SSAW} = 75.67\,\mathrm{m}^{-1}$. When the Fabry–Pérot (FP) resonance condition is satisfied, the SSAWs in the x direction interfere with each other to produce standing waves, which can be expressed as

$$\frac{\sqrt{2}}{2}k_{SSAW}L = m\pi + \gamma\,(m = 1,\,2,\,3\ldots), \tag{2}$$

where L is the total length of the structure, and m is the order of the resonance mode. γ is the phase shift caused by the edge of the structure. When we set $L = 20$ cm, $m = 3$, we can get the reflection phase $\gamma = 0.4\pi$. The calculated reflection phase γ is plugged into the formula $\frac{\sqrt{2}}{2}k_{SSAW}l = \pi + \gamma$, so the length $l = 82$ mm. It can be observed that the arrows of the velocity field are distributed in a regular configuration on the surface of the sample, and the direction of the arrows in the same row is constantly flipped from 0 to $\frac{\pi}{2}$, forming Néel-type meron, or from $\frac{\pi}{2}$ to π, forming Néel-type antimeron.[34] The absolute value of the out-of-plane sound velocity field reaches its maximum value at the center of each meron (or antimeron) and gradually decreases. The topological properties of the vector field configuration can be characterized by the skyrmion number S,[18]

$$S = \frac{1}{4\pi}\iint \vec{n}\cdot\left(\frac{\partial\vec{n}}{\partial x}\times\frac{\partial\vec{n}}{\partial y}\right)dxdy, \tag{3}$$

where $\vec{n} = \frac{Re(\boldsymbol{v})}{|Re(\boldsymbol{v})|}$. In our meron lattice, S can be defined by the distribution of the sound velocity field. The two-dimensional (2D) velocity field vector can be expressed as a distribution spread out by a parameterized sphere by latitude $\alpha(\varphi)$ and longitude $\beta(\rho)$, as shown in Fig. 2(c). A vector on a three-dimensional sphere can be defined as (r, β, φ), which corresponds to a vector on a two-dimensional plane by the coordinates (ρ, φ). Therefore, S can also be represented as the following:[14]

$$S = \left(\frac{1}{2}\int_0^R \sin\beta(\rho)d\rho\right)\left(\frac{1}{2\pi}\int_0^{2\pi}\frac{d\alpha(\varphi)}{d\varphi}d\varphi\right) = p\cdot m, \tag{4}$$

where $p = \frac{1}{2}[\cos\beta(\rho)]|_{\rho=0}^{\rho=R}$, defining the polarity and $m = \frac{1}{2\pi}[\alpha(\varphi)]|_{\varphi=0}^{\varphi=2\pi}$, defining the vorticity. From the velocity field distribution in the unit cell of the meron lattice as shown in Fig. 2(c), we can see that the velocity field arrow rotates from the vertical direction at the center to the horizontal direction at the edge. According to the mapping relation, the meron mode corresponds to a half

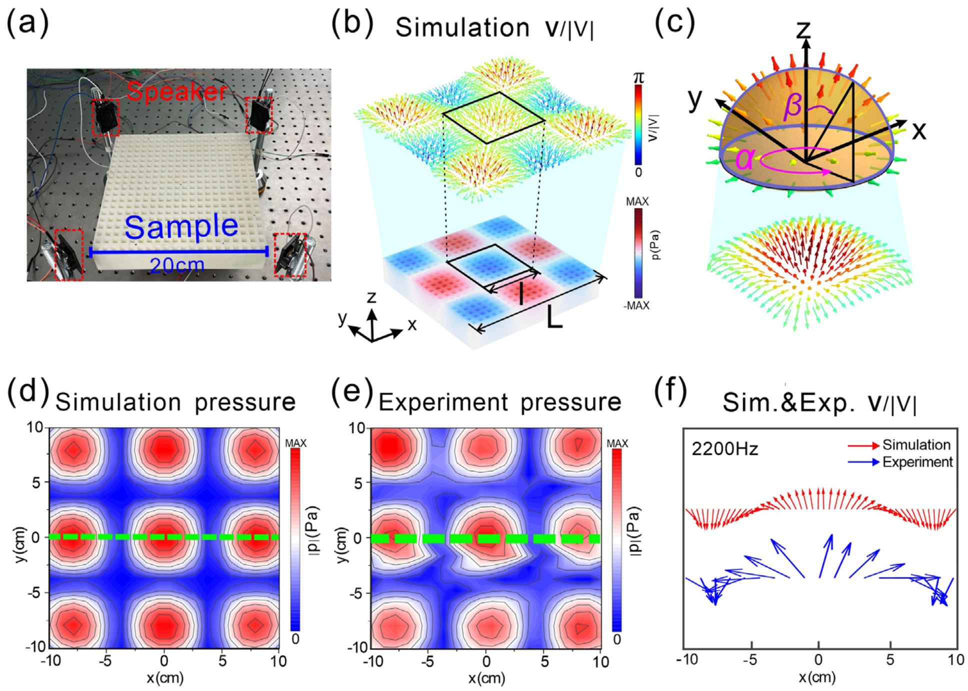

FIG. 2. Acoustic meron simulation and experimental measurement of sound pressure distribution and velocity field distribution. (a) Schematic diagram of the experimental setup. (b) Simulation diagram of the meron mode formed by the acoustic velocity field. The direction of the acoustic velocity field is shown by the arrow. (c) The mapping relationship between two-dimensional plane and three-dimensional sphere. (d) and (e) The simulated and experimentally measured sound pressure fields are distributed on the surface of the sample. (f) The arrows of the simulated (red arrows) and experimental (blue arrows) velocity fields are shown on the sample surface at the green dotted lines in (d) and (e).

parameterized sphere, and the skyrmion number of a meron in the lattice is $S = 0.5$ for the meron mode and $S = -0.5$ for the antimeron mode. We draw the boundary of $V_z = 0$ by using COMSOL software and calculate the skyrmion number integral of meron within the central boundary, and the skyrmion number value is 0.495, close to 0.5. In fact, the physical mechanism behind the meron lattice is the superposition of two pairs of counter propagating SSAWs along x and y directions, the velocity field z component of the meron lattice can be theoretically expressed as

$$V_z = \frac{2p_0}{\rho_0\omega} e^{-k_z z} k_z \left[\cos\left(\frac{\sqrt{2}}{2} k_{SSAW} x\right) + \cos\left(\frac{\sqrt{2}}{2} k_{SSAW} y\right)\right], \quad (5)$$

where p_0 is the incident wave amplitude, and ρ_0 is the mass density of air. From Eq. (5), we can find that the V_z will be the largest at the center of the meron unit cell [see Fig. 2(c)] for $\frac{\sqrt{2}}{2} k_{SSAW} x = 0$ and $\frac{\sqrt{2}}{2} k_{SSAW} y = 0$, while the z component will be zero at the meron boundary for $\frac{\sqrt{2}}{2} k_{SSAW} x = \pm\pi/2$ and $\frac{\sqrt{2}}{2} k_{SSAW} y = \pm\pi/2$.

Next, we observe the meron lattice in the experiment. Four speakers serve as point sources placed 1 cm around the sample. The sine wave signal generated by the signal generator (AFG1022, Tektronix) is amplified in the power amplifier (CPA2400, SinoCinetech) and passed through a splitter box (FM02–12D, Tatsukawa) to drive the speakers. We use a free-field microphone (MPA416, BSWA TECH) to measure the pressure above the sample with intervals of 0.3 cm along the surface of each cell of the lattice and record the sound pressure intensity.

The simulated and experimental results are shown in Figs. 2(d) and 2(e). In order to characterize the distribution of the meron mode, we measure the velocity field distribution at the green dotted line in Figs. 2(d) and 2(e) by using a WL-AVS-3D vector microphone.[18,35] We normalize the components of the measured sound velocity field V_x and V_z and display the processed data in the x-z plane. In fact, due to the high symmetry of the tetragonal lattice, the velocity field distribution on the y-z plane is no different from that on the x-z plane. The results of numerical simulation and experimental measurement are shown in Fig. 2(f). The red arrow at the top shows the results of the simulation, and the blue arrow at the bottom shows the results of the experiment. It can be seen that the direction of the velocity field is continuously rotated from 0 to $\frac{\pi}{2}$, which is consistent with the simulated results, and proves the meron lattice pattern.

In this section, we will show how to manipulate the acoustic meron lattice shift by controlling the phase and amplitude difference between two pairs of speakers. We place point source at four corners about 1 cm away from the sample to excite the meron mode at frequency $f = 2200$ Hz. The phases of the four speakers are numbered as Φ_n with $n = 1, 2, 3, 4$. When the phase $\Phi_1 = \frac{\pi}{2}$ and $\Phi_3 = -\frac{\pi}{2}$, with the phase Φ_2 and Φ_4 remaining at 0, the simulated out-of-plane sound velocity field V_z and the sound pressure field distribution on the structure surface are shown in Fig. 3(a). The meron lattice moves along the purple arrow (diagonal direction of the x and y axes) with a distance of $\lambda_{SSAW}/4$.

Similarly, when the phases $\Phi_2 = \frac{\pi}{2}$ and $\Phi_4 = -\frac{\pi}{2}$, with the phases Φ_1 and Φ_3 remaining 0, we can see that the arrow representing the

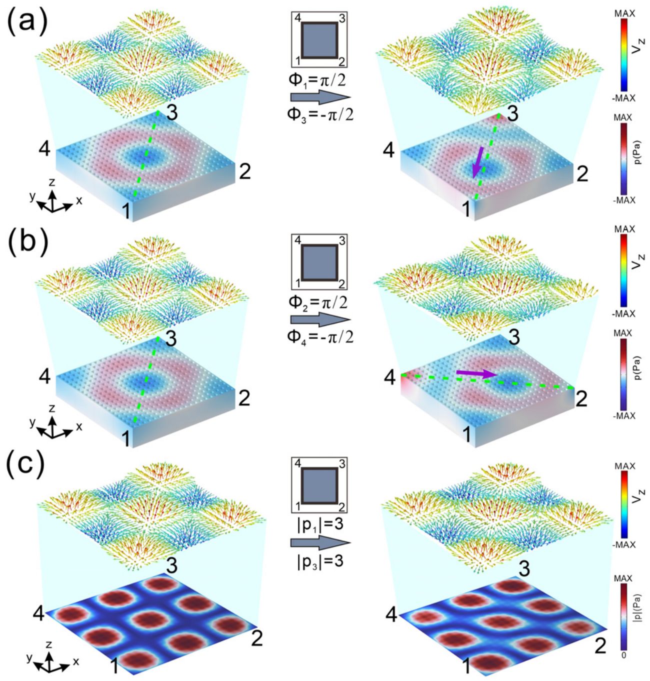

FIG. 3. Manipulation of acoustic meron lattices by adjusting phase and amplitude of the sound waves of the two pairs of speakers at the boundary. (a) The meron lattice can be moved diagonally along the x and y axes by changing the phase of $n = 1$ and $n = 3$ from 0 to $\frac{\pi}{2}$ and $-\frac{\pi}{2}$. The purple arrow indicates the direction of movement. (b) Similarly, the meron lattice can move in the opposite diagonal direction of the x and y axes by changing the phase of $n = 2$ and $n = 4$, from 0 to $\frac{\pi}{2}$ and $-\frac{\pi}{2}$, respectively. (c) Deformation of acoustic meron lattice by increasing the amplitude on the same side.

sound velocity field has been moved up by a distance of $\lambda_{SSAW}/4$ along the purple arrow (the opposite diagonal direction of the x and y axes). The distribution of sound pressure field and sound velocity field on the surface of the structure before and after the movement are shown in Figs. 3(a) and 3(b). The physical mechanism is that adding the $\frac{\pi}{2}$ phase by the loudspeakers along the diagonal direction of x and y will add a phase factor into x and y components, Eq. (5). Thus, the velocity field components V_z will move diagonally along x and y directions. The arrow representing the sound velocity field still conforms to the meron model after changing the phase, which confirms the motion of the meron lattice. Moreover, we can also deform the meron lattice by controlling the amplitude of the sound sources on the same side. We adjusted the amplitudes of one- and three-sided speakers by a factor of 3, and the resulting meron shape is shown in Fig. 3(c). It can be seen that the meron lattice is gradually stretched and combined with other merons, eventually leading to large deformation.

To demonstrate the topological property of the meron lattice against the structure defect, we introduce the defect of the purple frame of Fig. 4(b) to break the squared structure. Through the simulation calculation and comparison, it is found that the distribution of the sound velocity field of the lattice after the introduction of defects will not change significantly even if the surface sound pressure field has some changes. The defects are placed at $x = 2$ and 3 cm, and we simulate the sound pressure diagram at the red dotted line in Fig. 4(a) and the blue

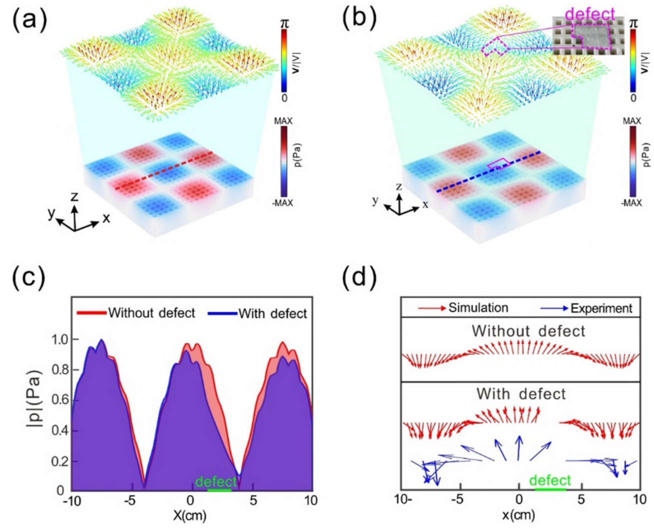

FIG. 4. Robustness of the acoustic meron lattice. (a) and (b) The meron model generated on the surface of the structure and the comparison diagram with the defect. (c) and (d) Sound pressure comparison diagram with and without defect and simulation and experiment diagram of sound velocity field. The green solid line represents the defect location along the blue dashed line on the sample surface in (b).

dotted line in Fig. 4(b), and the specific details are shown in Fig. 4(c). The introduction of defects in the hole causes the sound pressure distribution to be asymmetrical along the x direction, and the distribution of the overall sound pressure field on the surface is slightly distorted. However, the distribution of the sound velocity field is not greatly affected, and it changes only slightly near the defect. We use the same measurement method to measure the sound velocity field data of the blue dotted line in Fig. 4(b) on the surface of the structure, and then normalize the measured data and draw it in vector form. The simulation and experimental results are shown in Fig. 4(d). Based on the fact that the arrow representing the sound velocity field does not change much after the introduction of the defect, the results show that the meron lattice has good robustness to structure changes.

Summarily, we theoretically propose and experimentally observe that the Néel-type meron lattice configuration of acoustic velocity fields can be realized on a squared metastructure. The spoof acoustic surface waves with the evanescent nature are supported on the structure surface interfere to form the meron and antimeron pattern of acoustic velocity field distributions. Furthermore, we also observe that the meron lattice can be moved and shaped by controlling the phase and amplitude difference between the acoustic sources. The acoustic meron texture provides potential applications toward topologically robust ways to manipulate vectorial characteristics of the acoustic waves. In addition, the topological phase transition between trivial and nontrivial can be modulated by simply reducing or expanding the size or distance of unit cells in the lattice. By modulating the symmetry of the lattice, we may be able to get more physical applications of acoustic merons.[36–38]

This work was supported by the scientific research projects of colleges and universities in Anhui Province (Grant No. 2022AH040114) and the University Synergy Innovation Program of Anhui Province (Grant No. GXXT-2022-015).

AUTHOR DECLARATIONS

Conflict of Interest

The authors have no conflicts to disclose.

Author Contributions

Wan-Na Chen: Investigation (equal); Visualization (equal). **Wen-Jun Sun:** Formal analysis (equal); Investigation (equal); Validation (equal). **Zong-Qiang Sheng:** Supervision (equal); Writing – review & editing (equal). **Hong-Wei Wu:** Conceptualization (lead); Funding acquisition (lead); Project administration (lead); Supervision (lead); Writing – review & editing (equal).

DATA AVAILABILITY

The data that support the findings of this study are available on request from the corresponding author. The data are not publicly available due to its state restrictions such as privacy or ethical restrictions.

REFERENCES

[1]L. Xiong, Y. T. Li, D. Halbertal, M. Sammon, Z. Y. Sun, S. Liu, J. H. Edgar, T. Low, M. M. Fogler, C. R. Dean, A. J. Millis, and D. N. Basov, Nano Lett. **21**, 9256 (2021).
[2]J. Iwasaki, M. Mochizuki, and N. Nagaosa, Nat. Nanotechnol. **8**, 742 (2013).
[3]X. R. Lei, A. P. Yang, P. Shi, Z. W. Xie, L. P. Du, A. V. Zayats, and X. C. Yuan, Phys. Rev. Lett. **127**, 237403 (2021).
[4]Y. Tokura and N. Kanazawa, Chem. Rev. **121**, 2857 (2020).
[5]A. Ghosh, S. Yang, Y. Dai, Z. K. Zhou, T. Y. Wang, C. B. Huang, and H. Petek, Appl. Phys. Rev. **8**, 041413 (2021).
[6]C. F. Lu, B. Wang, X. Fang, D. P. Tsai, W. M. Zhu, Q. H. Song, X. Deng, T. He, X. Y. Gong, H. Luo, Z. S. Wang, X. H. Dai, Y. Z. Shi, and X. B. Cheng, Nano Lett. **24**, 104 (2024).
[7]M. Król, H. Sigurdsson, K. Rechcińska, P. Oliwa, K. Tyszka, W. Bardyszewski, A. Opala, M. Matuszewski, P. Morawiak, R. Mazur, W. Piecek, P. Kula, P. G. Lagoudakis, B. Piętka, and J. Szczytko, Optica **8**, 255 (2021).
[8]H. W. Wang and S. H. Fan, Phys. Rev. Lett. **131**, 263801 (2023).
[9]X. S. Wang, A. Qaiumzadeh, and A. Brataas, Phys. Rev. Lett. **123**, 147203 (2019).
[10]I. Kézsmárki, S. Bordács, P. Milde, E. Neuber, L. M. Eng, J. S. White, H. M. Rønnow, C. D. Dewhurst, M. Mochizuki, K. Yanai, H. Nakamura, D. Ehlers, V. Tsurkan, and A. Loidl, Nat. Mater. **14**, 1116 (2015).
[11]J. Jena, B. Göbel, T. P. Ma, V. Kumar, R. Saha, I. Mertig, C. Felser, and S. S. P. Parkin, Nat. Commun. **11**, 1115 (2020).
[12]A. Nayak, V. Kumar, T. P. Ma, P. Werner, E. Pippel, R. Sahoo, F. Damay, U. Rößler, C. Felser, and S. S. P. Parkin, Nature **548**, 561 (2017).
[13]S. Tsesses, E. Ostrovsky, K. Cohen, B. Gjonaj, N. H. Lindner, and G. Bartal, Science **361**, 993 (2018).
[14]Y. J. Shen, Q. Zhang, P. Shi, X. C. Du, A. V. Yuan, and Zayats, L. P., Nat. Photonics **18**, 15 (2023).
[15]Y. J. Shen, E. C. Martínez, and C. R. Guzmán, ACS Photonics **9**, 296 (2022).
[16]Q. Zhang, Z. W. Xie, L. P. Du, P. Shi, and X. C. Yuan, Phys. Rev. Res. **3**, 023109 (2021).
[17]Q. Zhang, Z. W. Xie, P. Shi, H. Yang, H. R. He, L. P. Du, and X. C. Yuan, Photonics Res. **10**, 947 (2022).
[18]H. Ge, X. Y. Xu, L. Liu, R. Xu, Z. K. Lin, S. Y. Yu, M. Bao, J. H. Jiang, M. H. Lu, and Y. F. Chen, Phys. Rev. Lett. **127**, 144502 (2021).
[19]P. Hu, H. W. Wu, W. J. Sun, N. Zhou, X. Chen, Y. Q. Yang, and Z. Q. Sheng, Appl. Phys. Lett. **122**, 022201 (2023).
[20]W. J. Sun, H. W. Wu, P. Hu, N. Zhou, X. Chen, Y. Q. Yang, and Z. Q. Sheng, Appl. Phys. Lett. **122**, 202201 (2023).
[21]L. Y. Cao, S. Wan, Y. Zeng, Y. F. Zhu, and B. Assouar, Sci. Adv. **9**, eadf3652 (2023).
[22]D. A. Smirnova, F. Nori, and K. Y. Bliokh, arXiv:2308.03520 (2023).
[23]X. Z. Yu, W. Koshibae, Y. Tokunaga, K. Shibata, Y. Taguchi, N. Nagaosa, and Y. Tokura, Nature **564**, 95 (2018).
[24]Z. L. Deng, T. Shi, A. Krasnok, X. P. Li, and A. Alù, Nat. Commun. **13**, 8 (2022).
[25]C. Guo, M. Xiao, Y. Guo, L. Q. Yuan, and S. H. Fan, Phys. Rev. Lett. **124**, 106103 (2020).
[26]C. Shi, R. Zhao, Y. Long, S. Yang, Y. Wang, H. Chen, J. Ren, and X. Zhang, Nat. Sci. Rev. **6**, 707 (2019).
[27]L. Burns, K. Y. Bliokh, F. Nori, and J. Dressel, New J. Phys. **22**, 053050 (2020).
[28]Y. Long, D. Zhang, C. Yang, J. Ge, H. Chen, and J. Ren, Nat. Commun. **11**, 4716 (2020).
[29]K. Y. Bliokh and F. Nori, Phys. Rev. B **99**, 020301 (2019).
[30]K. Y. Bliokh and F. Nori, Phys. Rev. B **99**, 174310 (2019).
[31]Y. Long, C. W. Yang, H. Chen, and J. Ren, Phys. Rev. Appl. **19**, 064053 (2023).
[32]R. D. Muelas-Hurtado, K. Volke-Sepúlveda, J. L. Ealo, F. Nori, M. A. Alonso, K. Y. Bliokh, and E. Brasselet, Phys. Rev. Lett. **129**, 204301 (2022).
[33]N. Cselyuszka, M. Sečujski, N. Engheta, and V. C. Bengin, New J. Phys. **18**, 103006 (2016).
[34]S. Hayami and R. Yambe, Phys. Rev. B. **104**, 094425 (2021).
[35]H. Ge, S. Liu, X. Y. Xu, Z. W. Long, Y. Tian, X. P. Liu, M. H. Lu, and Y. F. Chen, Phys. Rev. Lett. **131**, 014001 (2023).
[36]Z. W. Zhang, H. Y. Long, C. Liu, C. Shao, Y. Cheng, X. J. Liu, and J. Christensen, Adv. Mater. **31**, 1904682 (2019).
[37]X. X. Wu, X. Li, R. Y. Zhang, X. Xiang, J. X. Tian, Y. Z. Huang, S. X. Wang, B. Hou, C. T. Chan, and W. J. Wen, Phys. Rev. Lett. **124**, 075501 (2020).
[38]Z. C. Yu, Z. W. Zhang, H. X. Wang, W. Xiong, Y. Cheng, and X. J. Liu, New J. Phys. **24**, 053009 (2022).